Intrinsic Vibrational Coherence in Face-Centered Cubic Supra-Crystals of Silver Nanocrystals: Raman Scattering Measurements

A. Courty,[†] P. A. Albouy,[‡] A. Mermet,[§] E. Duval,[§] and M. P. Pileni*,[†]

Laboratoire des Materiaux Mésoscopiques et Nanométriques, UMR-CNRS 7070, Université Pierre et Marie Curie, BP 52, 4 place Jussieu, 75252 Paris Cedex 05, France, Laboratoire de Physique des Solides, UMR-CNRS 8502, Université Paris-Sud, Bât 510, 91405 Orsay, France, and Laboratoire de Physico-Chimie des Matériaux Luminescents, UMR-CNRS 5620, Université Lyon I, 69622 Villeurbanne Cedex, France

Received: March 15, 2005; In Final Form: July 12, 2005

The ordering of silver nanocrystals is tuned from amorphous aggregates to highly well-ordered, face-centered cubic supra-crystals, using various substrates and controlling their temperature to obtain this. Low-frequency Raman scattering, for the first time, demonstrates vibrational coherence in fcc supra-crystals of nanocrystals. This is shown by a narrowing of the peak corresponding to the quadrupolar modes of the nanocrystals. However, this is obtained when the supra-crystals are smaller than the excitation wavelength. When the supra-crystals are larger, the narrowing cannot be observed. Furthermore, for any size of the supra-crystals, a shift to low frequency of the Raman peak due to the Lorentz field effect is seen.

I. Introduction

These past few years it has been well demonstrated that, due to dipolar interactions, collective optical,[1−5] magnetic[1,6−8] and transport[1,9,10] properties emerge from the ordered periodic arrangement of nanocrystals in 2D superlattices.

A crystal is characterized by an atomic order in 3D symmetry. Manipulation of nanocrystals having low size distribution permits the building of a regular arrangement of nanometer scale spheres at the mesoscopic scale.[1,11−17] These supra-crystals, characterized by an face-centered cubic (fcc) structure, are a new class of materials. Of particular interest is the question of whether new collective properties emerge from the ordered periodic arrangement of nanocrystals in supra-crystals. We discovered that self-organization of nanocrystals in fcc supra-crystals plays a mechanical role in the control of cobalt nanocrystals' organization in columns.[18,19] An intrinsic dynamic behavior (lattice vibrations) that is absent in noncrystalline solids composed of nanoparticles is observed.[20] According to news and views in *Nature Materials*,[21] the importance of this discovery establishes for the first time the emergence of a new collective of properties in 3D supra-crystals. Other intrinsic properties seem to emerge as the oxidation of cobalt nanocrystals is prevented and their stability protected by the self-organization of nanocrystals.[22]

Up to now, most of the publications report on Raman scattering of metallic particles embedded in various kinds of insulating matrixes.[23−27] The coupling between particles can be thus neglected. Nevertheless, very recently, low-frequency Raman measurements have been made on 2D self-organized silver nanocrystals.[28] The observed Raman spectra are similar to those obtained for isolated silver nanoparticles embedded in a matrix. Hence, no coupling effects have been shown. However, in 2D organizations, the substrate effect has to be taken into account, and it could prevent coupling between particles. Thus, these results do not show whether self-organized nanocrystals induce collective vibrational properties or not.

This paper reports the intrinsic physical properties due to the self-organization of 5 nm silver nanocrystals in fcc superlattices. For this, the vibrational properties of 3D silver nanocrystal assemblies of different degrees of ordering (from disordered to fcc assemblies) are studied. By considering only 3D assemblies, the substrate effects on the Raman response are suppressed.

II. Experimental Section

II.1. Materials. Sodium di(2-ethyl-hexyl) sulfosuccinate, Na-(AOT), was from Sigma. Isooctane, hexane, and pyridine were from Fluka. Hydrazine and decanethiol were obtained from Prolabo (France). The materials were not further purified.

Silver di(2-ethyl-hexyl) sulfosuccinate, Ag(AOT), was prepared as described previously.[29]

II.2. Apparatus. Transmission electronic microscopy (TEM) and scanning electron microscopy (SEM) were performed with a JEOL 100 CX and a JSM-5510LV instrument, respectively.

Small-angle X-ray diffraction, SAXD, measurements were made with a rotating anode generator with a small size focus (0.2 mm × 0.2 mm, 50 kV, 30 mA). The optics consisted of a parabolic multilayer graded mirror followed by a bent nickel-coated mirror at right angles. These delivered a well-defined and intense parallel monochromatic beam. The sample was mounted on a rotation stage and its diffraction pattern recorded on photostimulable imaging plates. Vacuum pipes were inserted between the sample and the imaging plates.

Low-frequency Raman spectra were recorded with a five-grating monochromator. The high resolution and rejection rate of this arrangement make it possible to observe low-frequency Raman signals close to the Rayleigh line down to less than 2 cm^{-1}. The samples were illuminated with the 514.5 nm line of an Ar$^+$ laser, with an incidence angle close to $\pi/3$. Under these conditions, the excitation wavelength is close to the resonance of the broad dipolar plasmon excitation (2.9 eV for nanocrystals in solution in hexane), thereby ensuring plasmon resonant

* Corresponding author. E-mail: pileni@sri.jussieu.fr.
† Université Pierre et Marie Curie.
‡ Université Paris-Sud.
§ Université Lyon I.

Raman scattering. The scattered light was detected at about $\pi/2$ with respect to the incoming laser beam. Two different configurations are employed with the excitation and detection polarizations either parallel (VV) or perpendicular (HV) to each other.

II.3. Synthesis. Silver nanocrystals are synthesized by using a functionalized surfactant (silver di(2-ethyl-hexyl) sulfosuccinate, Ag(AOT))[30] and mixing two reverse micellar solutions. The first is 60% 0.1 M Ag(AOT) and 40% 0.1 M Na(AOT) solubilized in isooctane. The water content $w = [H_2O]/[AOT]$ is kept at 2. The second is 0.1 M NaAOT in isooctane with water replaced by hydrazine. Hydrazine is in excess, and its content, defined as $[N_2H_4]/[AOT]$, is kept at 1.44. Immediately after mixing these two reverse micelle solutions, silver nanocrystals are formed. Dodecanethiol (2 μL/cm^3) is then added to the solution, and a selective reaction with silver atoms at the interface of the particles takes place. To remove the AOT surfactant, ethanol is added to the solution. This induces the flocculation of the dodecanethiol-coated silver nanocrystals, and the resulting precipitate is then dispersed in hexane. To reduce the size distribution, a size-selected precipitation process[30] is used. At the end of the synthesis, silver nanocrystals, with 4.48 nm average diameter with a standard deviation σ of 0.71 nm, are obtained.

II.4. Nanocrystal Deposition Process. The used substrates are highly oriented pyrolitic graphite (HOPG) and amorphous carbon (a-C). The nanocrystals are deposited by horizontally immersing the substrate in 150 μL of the nanocrystal solution (at a fixed concentration of 2.2 10^{14} particles/mL). The solvent evaporation, which takes around 5 h, occurs at the desired substrate temperature, under hexane vapor pressure maintained close to saturation in the gas phase. Two depositions at 30 and 10 °C were made on an HOPG substrate. The same nanocrystals were also deposited on an a-C substrate at temperatures of 10 and 22 °C.

III. Results and Discussion

In a previous study, it was clearly demonstrated that controlling the substrate temperature and evaporation rate favors the formation of aggregates with long-range ordering.[31] Below we demonstrate that this long-range ordering of aggregates consists of supra-crystals in an fcc structure. In the following, the same nanocrystals (see synthesis above) are used.

III.1. Electron Microscopy and X-ray Diffraction: Supra-Crystalline Self-Organization. Let us first consider the deposition of 5 nm silver nanocrystals either on a-C (sample A) or HOPG (sample B) at 10 °C. With A (Figure 1A), the film appears to be rather homogeneous over a long range with small aggregates dispersed on the substrate (inset 1, Figure 1A). These aggregates are more or less spherical, and their average diameter is around 2 μm. The diffraction pattern of the film shows a circle at 0.89 nm^{-1} (Figure 2A) with an estimated intrinsic width of $q_{1/2} = 0.2$ nm^{-1} (Figure 3A). This is much larger than the experimental resolution (ca 0.03 nm^{-1}). The corresponding correlation length is crudely estimated at 14 nm by application of the Scherrer formula ($0.888\pi/\delta q_{1/2}$). This behavior clearly indicates that the silver nanocrystals are disordered arrangements on a-C. However, this does not exclude local arrangements of nanocrystals. Sample B shows a marked change on the film morphology (Figure 1B). Islands with 1.5 μm as average height and cracks are observed (inset 1, Figure 1B). The diffraction pattern shows a halo at 0.88 nm^{-1}, approximately hexagonal (Figure 2A). The estimated intrinsic halo width is $q_{1/2} \approx 0.15$ nm^{-1} (Figure 3B), and the corresponding correlation length is
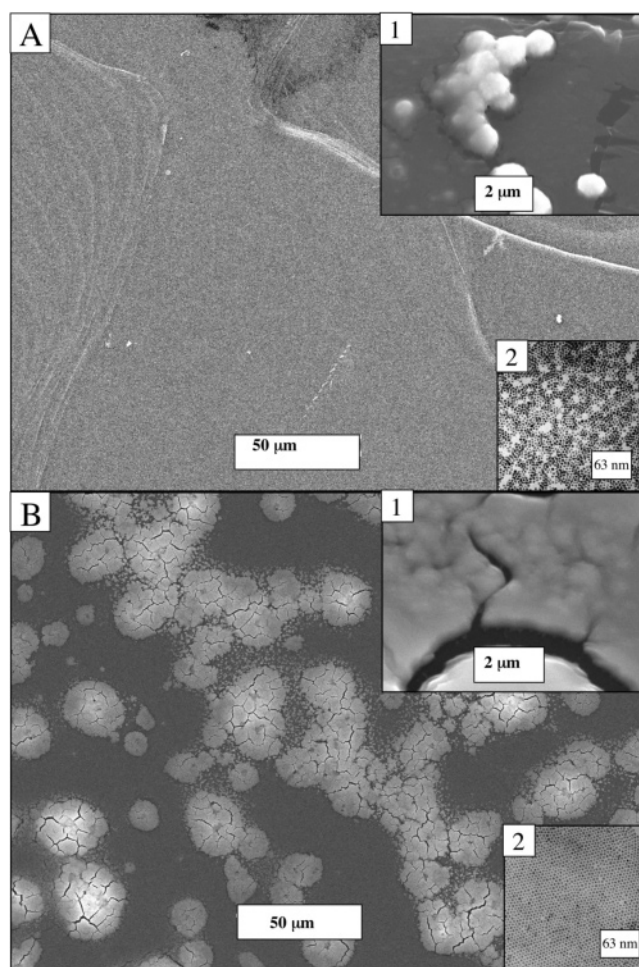
Figure 1. SEM patterns of 3D silver nanocrystal assemblies deposited at 10 °C on (A) an amorphous carbon substrate (sample A) (inset 1 shows a magnification of the surface and inset 2 shows the TEM pattern obtained by deposition of a drop of solution on the amorphous carbon) and (B) an HOPG substrate (sample B) (inset 1 shows a magnification of the surface and inset 2 shows the TEM pattern obtained by deposition of a drop of solution on the HOPG).

18 nm. This indicates a better arrangement on HOPG than on a-C. Nevertheless, in both cases, because the diffraction pattern shows a diffused halo, the arrangements of silver nanocrystals can be considered as disordered. We must note that a similar slight change in the local arrangement is observed by deposition of a drop of solution at room temperature. While the arrangement on a-C appears more heterogeneous (inset 2, Figure 1A), it is more widespread on HOPG (inset 2, Figure 1B). However, a careful study shows that some zones on a-C are rather well organized.[32] As emphasized later, the more widespread arrangement does not necessarily imply a defect-free ordering, particularly in terms of vibrational coherence.

Deposition of silver nanocrystals on an a-C substrate at 22 °C (sample C) induces a change in the film morphology compared to that observed at 10 °C. Hence, isolated domains resembling pavements or paving stones with an average height of 3 μm (Figure 4A) and an average surface area of 2500 μm^2 are produced. From the higher resolution images (Figure 4A, inset), the surface of the domains appears rather smooth. The corresponding SAXD pattern (Figure 2C) shows clearly the signature of a crystallized material with two well-defined Bragg reflections (Figure 3C). The HWHM of the first order (0.05 nm^{-1}) is close to the resolution limit indicating long-range ordering of the nanocrystals perpendicular to the surface. The

Raman Scattering of Silver Nanocrystals

J. Phys. Chem. B, Vol. 109, No. 44, 2005 **21161**
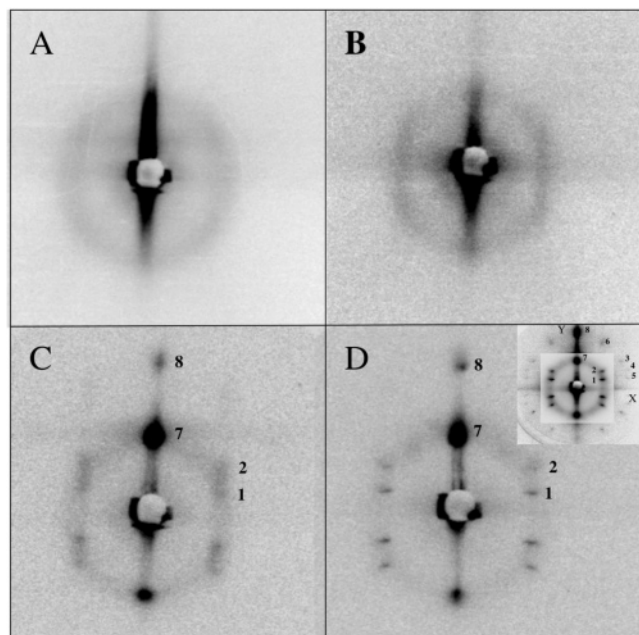
Figure 2. Diffractograms of 3D silver nanocrystal arrangements deposited on (A) an a-C substrate at 10 °C (sample A), (B) an HOPG substrate at 10 °C (sample B), (C) an a-C substrate at 22 °C (sample C), and (D) an HOPG substrate at 30 °C (sample D).

diffraction pattern shows slightly diffuse additional diffraction spots (numbered as 1 and 2 on Figure 2C). A comparison of observed and calculated diffraction spot coordinates enables indexing of the diffraction pattern. The spot coordinates are reported in Table 1, where reciprocal distances are converted into d-spacings using the well-known formula $q = 2\pi/d$, and fcc packing leads to very satisfactory agreement between the experimental data and calculated values. The calculations lead to an average coated diameter, $D_c = 7.9$ nm. This value includes the core diameter and a coating contribution. With the use of the core diameter value given by TEM, a coating contribution of 1.7 ± 0.4 nm is deduced. The average interparticle distance deduced from SAXD is thus 3.4 ± 0.8 nm. This is larger than that determined by TEM for the monolayers. This difference is attributed to the presence of defects inside the supra-crystals that are also taken into account by the SAXD technique.

By replacing amorphous carbon with HOPG and increasing the substrate temperature to 30 °C (sample D) a long-range ordering is observed. As with sample C, the SEM pattern shows pavement domains with an average height remaining at 3 μm (Figure 4B), whereas the average surface area of the domains is smaller (600 μm² instead of 2500 μm²). A higher substrate temperature explains this decrease in the average surface area of the domains during the solvent evaporation, which induces formation of a larger number of cracks in the silver film. The inset of Figure 4B shows a smoother surface than that observed for sample C (Figure 4A, inset), and the corresponding SAXD pattern confirms the signature of a crystallized material with two well-defined Bragg reflections (Figure 3D), and the HWHM of the first order (0.05 nm⁻¹) is close to the resolution limit. This indicates long-range ordering of the nanocrystals perpendicular to the surface. The diffraction pattern also shows well-defined additional diffraction spots (numbered as 1 and 2 on Figure 2D). This indicates an increase in the degree of in-plane ordering and thus an increase in the supra-crystals sizes. By tilting the sample by 10° numerous additional diffraction spots (numbered from 3 to 6) with different intensities are observed (Figure 2D, inset). For convenient visualization two different
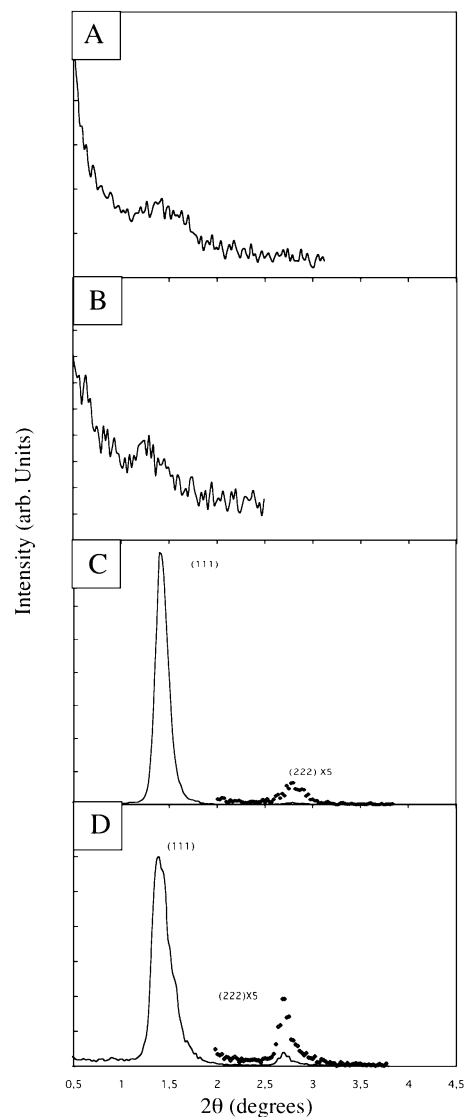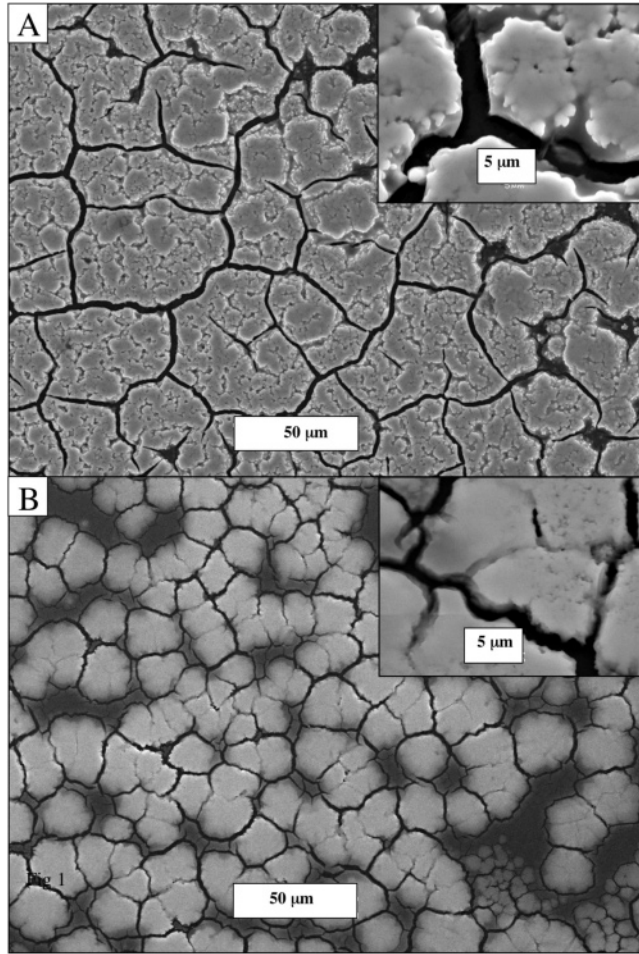

Figure 3. X-ray diffraction patterns of silver nanocrystal assemblies deposited on (A) an amorphous carbon substrate at 10 °C (sample A), (B) an HOPG substrate at 10 °C (sample B), (C) an amorphous carbon substrate at 22 °C (sample C), and (D) an HOPG substrate at 30 °C (sample D).

gray scales are used. These additional spots reveal that the in-plane orientation of the ordered nanocrystal domains is random. A comparison of observed and calculated diffraction spot coordinates enables indexing of the diffraction pattern as an fcc packing (Table 2). The calculated average coated diameter D_c stays almost unchanged with the nature of the substrate (7.9 nm).

From these data it is concluded that both samples C and D are organized over a long range in an fcc structure. However, because of the better defined diffraction spots, it is easy to conclude that sample D supra-crystals present a better ordered arrangement with the formation of larger fcc supra-crystals domains than sample C. Hence, the nanocrystal size segregation during the supra-crystallization process is thus better in sample D than in sample C, inducing an increase of the correlation length and less defects in the supra-crystals.

From these data is it demonstrated that it is possible to tune the ordering of silver nanocrystals from disordered to fcc arrangements. In addition, the size of the ordered arrangements in fcc supra-crystals is also controlled (see summaries of the SAXD observations on the different samples in Table 3).

21162 *J. Phys. Chem. B, Vol. 109, No. 44, 2005*

Courty et al.

Figure 4. SEM patterns of 3D silver nanocrystal assemblies deposited on (A) an amorphous carbon substrate at 22 °C (sample C) (the inset shows a magnification of the surface) and (B) an HOPG substrate at 30 °C (sample D) (the inset shows a magnification of the surface.

TABLE 1: 3D Deposition of Silver Nanocrystals on an a-C Substrate at Room Temperature: Comparison between the Experimental and Calculated Coordinates of Diffraction Spots Assuming an fcc Structure

reflection label[a]	[hkl] indices	q_x (meas) $Å^{-1}$	q_x (calc) $Å^{-1}$	q_y (meas) $Å^{-1}$	q_y (calc) $Å^{-1}$	d_{hkl} (meas) nm	d_{hkl} (calc) nm
1	1.1.−1	0.0353	0.0324	0.0905	0.0918	5.98	6.45
2	2.0.0	0.0619	0.0649	0.0868	0.0918	5.89	5.60
7	1.1.1	0.1025	0.0974	0	0	6.13	6.45
8	2.2.2	0.1996	0.1948	0	0	3.15	3.22

[a] See Figure 2C.

III.2. Low-Frequency Raman Scattering: Vibrational Coherence in Supra-Crystals. In a previous paper,[28] we demonstrated, by high-resolution electronic microscopy (HR-TEM), that the produced silver nanoparticles are highly crystallized. Indeed, multiple twinning particles (icosahedra and decahedra) and monocrystalline particles such as cuboctahedra are observed. This high crystallinity is confirmed by the intrananoparticle coherence observed by low-frequency Raman scattering. Figure 5 shows the Raman spectra, VV configuration, of samples A and B with a very intense peak at low frequency (around 8 cm^{-1}) and a less intense broader line at higher frequency (around 20 cm^{-1}) (the very strong line at −13.3 cm^{-1} is a plasma laser line reflected by the sample). A similar spectrum with a better signal-to-noise ratio was produced[28] when nanocrystals are organized in 2D superlattices. The lesser quality

TABLE 2: 3D Deposition of Silver Nanocrystals on an HOPG Substrate at 30 °C: Comparison between the Experimental and Calculated Coordinates of Diffraction Spots Assuming an fcc Structure[a]

reflection label[b]	[hkl] indices	q_x (meas) $Å^{-1}$	q_x (calc) $Å^{-1}$	q_y (meas) $Å^{-1}$	q_y (calc) $Å^{-1}$	d_{hkl} (meas) nm	d_{hkl} (calc) nm
1	1.1.−1	0.0338	0.0324	0.0936	0.0918	6.31	6.45
2	2.0.0	0.0644	0.0649	0.0905	0.0918	5.65	5.60
3	−1.3.1	0.0966	0.0974	0.1578	0.1590	3.39	3.37
4	1.1.3	0.1658	0.1623	0.0901	0.0918	3.33	3.37
5	2.2.−2	0.0644	0.0649	0.1803	0.1836	3.28	3.23
6	1.1.−3	0.0322	0.0324	0.1803	0.1836	3.43	3.37
7	1.1.1	0.1002	0.0974	0	0	6.27	6.45
8	2.2.2	0.198	0.1948	0	0	3.17	3.22

[a] The experimental coordinates have been determined from the diffraction pattern obtained for a tilt angle around 10° of the sample. [b] See Figure 2D.

TABLE 3: Summaries of the Observations Made through SAXD on the Different Samples

sample	substrate	temperature	type of 3D arrangement
A	a-carbon	10 °C	disordered
B	HOPG	10 °C	disordered
C	a-carbon	22 °C	"supra"-crystal
D	HOPG	30 °C	"supra"-crystal, large domains

of the 3D Raman spectra may be due to the roughness of the 3D nanocrystal deposition inducing some stronger elastic scattering. It was shown that the intense line at low frequency is due to quadrupolar vibration modes and the less intense line at higher frequency is due to spherical breathing mode. In the following, we concentrate on the HV spectrum, selecting the Raman scattering peak due to the quadrupolar modes.

Because the samples described above are prepared with the same nanocrystals having the same average size and distribution
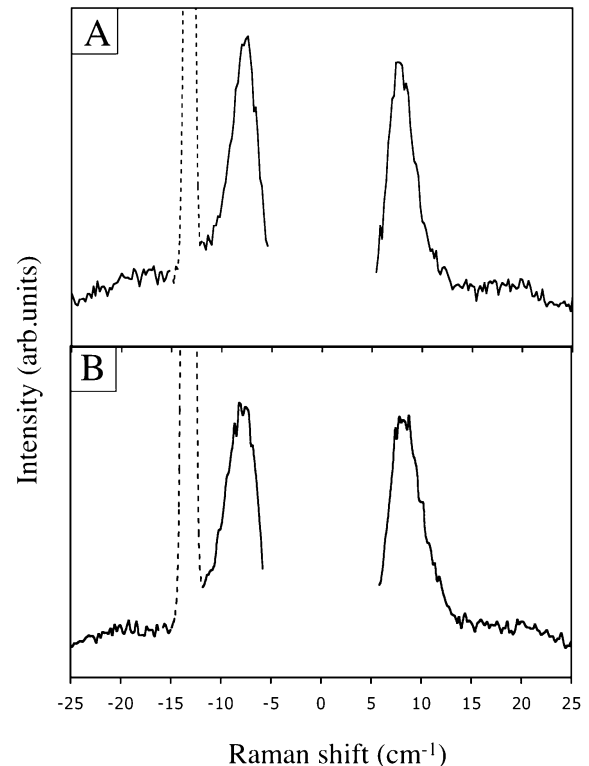
Figure 5. Low-frequency Raman spectra, obtained in VV configuration, of silver nanocrystals deposited at 10 °C on (A) an amorphous carbon substrate and (B) an HOPG substrate. The sharp dashed lines at −13.3 cm^{-1} are plasma laser lines reflected by the samples.

Raman Scattering of Silver Nanocrystals

*J. Phys. Chem. B, Vol. 109, No. 44, 2005* **21163**
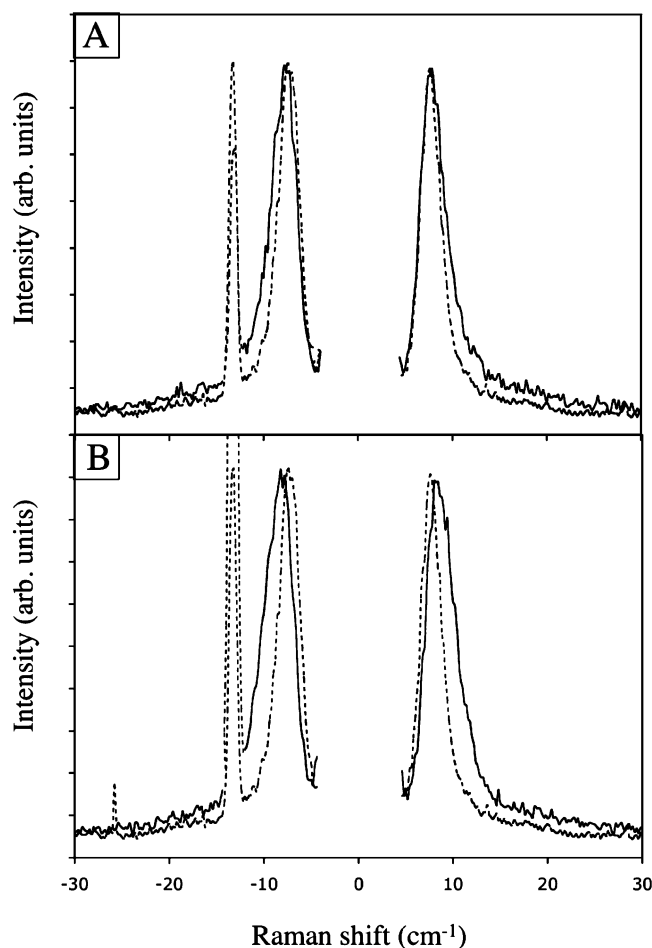
Figure 6. Low-frequency Raman spectra, obtained in HV configuration, of silver nanocrystals deposited on (A) an amorphous carbon substrate at 10 °C (sample A, solid line) and on the same substrate at 22 °C (sample C, dashed line) and (B) an HOPG substrate at 10 °C (sample B, solid line) and on an amorphous carbon substrate at 22 °C (sample C, dashed line).

and because the amount of nanocrystals deposited are the same, the comparison of the Raman scattering spectra obtained with the various samples can be attributed to the change in their ordering on mesoscopic scale.

III.2.a. Low-Frequency Raman Scattering from Disordered Assemblies of Nanocrystals. The solid lines in Figure 6, parts A and B, show the HV Stokes−anti-Stokes Raman spectrum of samples A and B, respectively. As observed previously with similar systems,[23,24] the quadrupolar modes appear as sharp intense lines. In fact, low-frequency Raman scattering by vibrations of silver nanocrystals is intense when the incident light energy is in resonance with that of the electronic dipolar plasmon.[25] For spherical nanocrystals larger than ∼1 nm, these vibrations are described by modeling the nanocrystal with a continuum nanosphere of a diameter D equal to the size of the nanocrystal[23] and using the longitudinal, V_l, and transversal, V_t, sound velocities of bulk Ag. From the theory of sphere oscillations by Lamb,[33] the vibrations are characterized by the quantum numbers n and l, as for spherical harmonics, and the vibrational frequencies are given by the following simple equation:

$$\nu = \frac{S_{ln}V_t}{D} \qquad (1)$$

where S_{ln} depends on the ratio V_l/V_t. Only spherical ($l = 0$) and
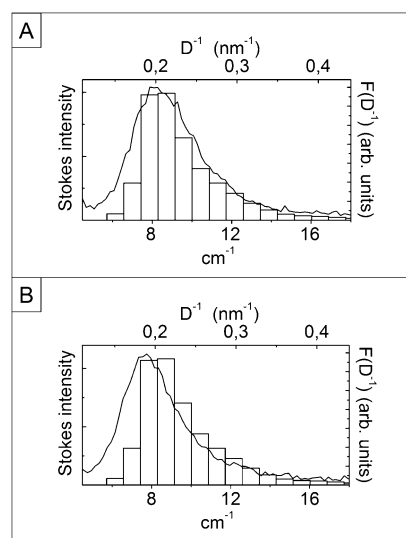
Figure 7. Comparison of the Stokes line shapes of (A) sample B (deposition on an HOPG substrate at 10 °C) and (B) sample A (deposition on amorphous carbon at 10 °C) with the inverse nanocrystal diameter distribution $F(D^{-1})$.

quadrupolar ($l = 2$) modes are observed by Raman scattering. This was confirmed from experiments and theoretical considerations.[24] While the latter modes are easily detected, due to their coupling with the dipolar plasmon, the observation of the spherical modes requires a narrow size distribution of the nanocrystals.[26,27] Figure 7A compares the Stokes line shape of sample B with the inverse size distribution $F(D^{-1})$. From eq 1, a good matching of the two curves is obtained with an average sound velocity $V_t = 1500$ m/s, taking $S_{ln} = 0.83$, the theoretical value which corresponds to the V_l/V_t ratio of silver. Note that this sound speed value is close to that in bulk silver (1660 m/s). According to previous findings,[27] the relatively good agreement between the inverse size histogram and the Raman line shape demonstrates the intrananoparticle coherence, i.e., nanocrystallinity, and not internanocrystal coherence (or supra-crystallinity). This is confirmed by the SAXD pattern of sample B (Figure 2B) showing a broad diffusing ring typical of a disordered arrangement. Conversely to what is observed with sample B, the sample A Raman line shape does not fit very well with the inverse size distribution (Figure 7B). As discussed below, this discrepancy testifies to a small effect of organization (i.e., vibrational coherence), which is not revealed by SAXD but is slightly observed in 2D superlattices. In this respect, vibrational spectroscopy is a more sensitive probe.

For an isolated particle, the intensity of Raman scattering by a particle vibration changes with the degree of spatial coherence, or crystallinity, inside the Ag nanocrystals. This intensity, $I^{(1)}(\nu)$, for total intrananocrystal coherence (i.e., good nanocrystal crystallinity), without internanocrystal coherence, is given by the following expression (to simplify, the indices for the components of the intensity tensor were suppressed) for Stokes Raman scattering:[35]

$$I^{(1)}(\nu) = \frac{n(\nu) + 1}{\nu}[\delta^{(1)}\alpha(\nu)]F(\nu) \qquad (2)$$

where $n(\nu)$ is the Bose factor, $\delta^{(1)}\alpha(\nu)$ is the polarizability fluctuation of an isolated nanocrystal, and $F(\nu)$ is the normalized frequency distribution, which is related to the normalized inverse size distribution, $F(D^{-1})$, through eq 1 ($F(\nu) \, d\nu = F(D^{-1}) \, dD^{-1}$). Obviously, $\delta^{(1)}\alpha(\nu)$ is proportional to the number of atoms, N_D, in a nanocrystal when there is intrananocrystal coherence.
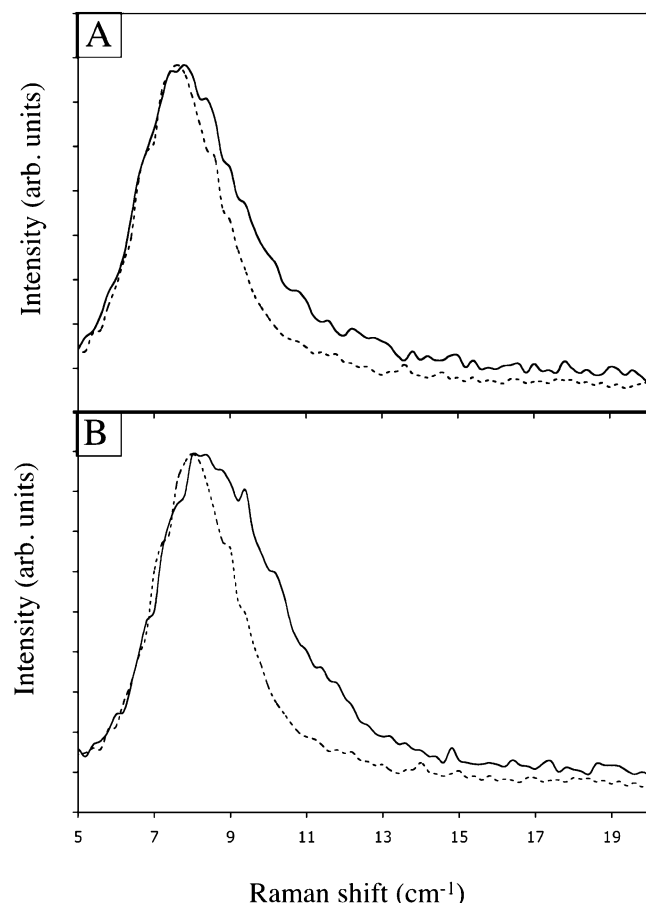
Figure 8. Superposition of Stokes line shapes after horizontal shifting of (A) sample A (deposition on an amorphous carbon substrate at 10 °C) and sample C (deposition on an amorphous carbon substrate at 22 °C); (B) sample B (deposition on an HOPG substrate at 10 °C) and sample C.

Because of the frequency dependence of the different terms in eq 2, the scatter intensity of an assembly of nanocrystals is proportional to the frequency distribution:

$$I^{(1)}(\nu) \propto F(\nu) \qquad (3)$$

This was already demonstrated previously[27] and confirmed in Figure 7A.

III.2.b. Low-Frequency Raman Scattering from Supra-Crystals: Vibrational Coherence. Figure 6A compares the HV Raman spectra of samples A and C. The Raman peak corresponding to the sample C quadrupolar modes is very slightly shifted toward a low frequency compared to that of the sample A Raman peak with a decrease of its width. This narrowing of the peak (Figure 8A) is better observed by shifting the Raman peaks of samples A and C to a given frequency. Similar behavior is observed by comparing the Raman spectra of samples B and C, i.e., a shift of the Raman peak of sample A toward a low frequency (Figure 6B) and decrease of its width (Figure 8B). Note that this narrowing effect appears slightly more pronounced with sample B than with sample A.

The Raman spectra of samples B and D are compared in Figure 9. A low-frequency shift of the Raman peak is observed (Figure 9A) while the line shape is identical for both samples (Figure 9B).

From the above results, it appears that the narrowing of the Raman quadrupolar peak is only visible for the small "supra"-crystals (sample C) and disappears when the supra-crystals are large (sample D). To explain this change in the behavior with
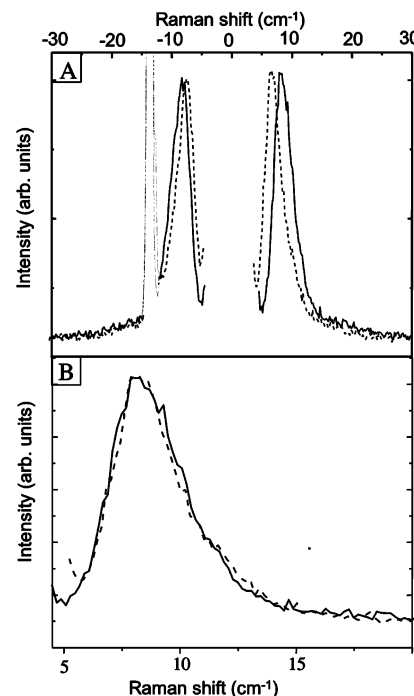
Figure 9. (A) Low-frequency Raman spectra, obtained in HV configuration, of silver nanocrystals deposited on an HOPG substrate at 10 °C (solid line, sample B) and at 30 °C (dashed line, sample D). (B) Superposition of both line shapes after horizontal shifting.

the ordering of nanocrystals two effects have to be taken into account: the effect of the Lorentz field and that of vibrational coherence in a supra-crystal. The theoretical model of low-frequency Raman scattering by supra-crystals is developed in ref 35. In the present paper, we extract the physical meaning from the theory to explain the effect of coherence on the quadrupolar Raman peak and to interpret the experimental results.

III.2.b.i. Effect of the Lorentz Field. The electromagnetic field that is induced on each nanocrystal by the (vibration-fluctuating) electric dipoles of the neighboring nanocrystals organized in fcc supra-crystals changes the nanocrystal polarizability fluctuation, $\delta\alpha(\nu)$. As noted in ref 35, this effect exists if the electromagnetic fields induced by the different neighboring nanocrystals are in phase. Consequently, the electromagnetic coherence is necessary for this effect, as occurs with the supra-crytalline arrangements. In this case, the nanocrystal polarizability fluctuation, $\delta\alpha(\nu)$, in a supra-crystal, is equal to the polarizability fluctuation of an isolated nanocrystal, $\delta^{(1)}\alpha(\nu)$, multiplied by the factor $L(\nu)$ that accounts for the Lorentz field. $L(\nu)$ is dependent on the size D of the nanocrystals in the supra-crystal and, thus, on ν through eq 1: $\delta\alpha(\nu) = L(\nu)\delta^{(1)}\alpha(\nu)$.

III.2.b.ii. Effect of Vibrational Coherence. The vibrational coherence among the nanocrystals in a supra-crystal is established due to the weak interdigitization of the thiol chains. The van der Waals bonding between thiol chains is too weak to have a measurable effect on the vibrational frequencies of nanocrystals. However, it is sufficient to establish a correlation between the vibrating nanocrystals so that they vibrate coherently in a supra-crystal. The quadrupolar modes in a supra-crystal are like nondispersive optical modes.

Before expressing the Raman intensity of a sample, in which the nanocrystals are organized into supra-crystals, it is remarked that (i) supra-crystallization (without defects) is possible only with same nanocrystals size; (ii) the number of nanocrystals (vibrating at the frequency ν) in a supra-crystal is likely

Raman Scattering of Silver Nanocrystals

J. Phys. Chem. B, Vol. 109, No. 44, 2005 **21165**

proportional to $F(\nu)$; (iii) the volume illuminated by the incident laser beam is much larger than the volume of a supra-crystal so that the size distribution of the scattering nanocrystals does not change with the degree of self-organization.

A clear distinction between large and small (size $\leq\lambda/10$, λ being the light wavelength) supra-crystals has to be made.

(A) In the case of *large supra-crystals*, the light is scattered by propagating modes characterized by the momentum **k** and a frequency ν. In the Raman transition by these propagating modes, the energy and also the momentum vector are conserved. Due to the Heisenberg indetermination relations, for given directions of incident and scattered lights, which determine the transfer momentum, there is not only one mode with a fixed momentum **k** which will scatter the light but also the modes in the interval Δ**k** that is determined by the Heisenberg relations. It is easily found that the number of these propagating modes, which scatter the light, is inversely proportional to the supra-crystal volume, i.e., to the inverse of the number of nanocrystals in the supra-crystal, $1/N_{SD}$. The Raman scattering intensity by a supra-crystal is proportional to the square of its polarizability fluctuation multiplied by the number of scattering vibration modes. The supra-crystal polarizability fluctuation at the frequency ν is equal to the nanocrystal polarizability fluctuation in the supra-crystal, $\delta\alpha(\nu)$, multiplied by N_{SD}. Therefore, from above, the intensity of Raman scattering from a large supra-crystal containing N_{SD} nanocrystals is proportional to $[N_{SD}L(\nu)\delta^{(1)}\alpha(\nu)]^2/N_{SD} = N_{SD}[L(\nu)\delta^{(1)}\alpha(\nu)]^2$. As noted above, the self-organization does not change the distribution of nanocrystals vibrating at the frequency ν. Furthermore, the number of nanocrystals, N_{SD}, vibrating at the frequency ν in a supra-crystal is proportional to the frequency distribution $F(\nu)$. Therefore, from eq 3, the intensity of Raman scattering from samples organized into large supra-crytals, $I^{(2)}(\nu)$, is given by the following expression:

$$I^{(2)}(\nu) \propto L^2(\nu)I^{(1)}(\nu) \qquad (4)$$

If it is considered that, to a first approximation, the only effect of $L(\nu)$ is to shift the Raman peak, then eq 4 shows that the Raman line-shape for large "supra"-crystals is the same as that for disordered or amorphous assemblies of nanocrystals. This is clearly observed in Figure 9B for samples B and D.

(B) In the case of *small supra-crystals* (size $\leq\lambda/10$), the light is scattered by stationary modes in the supra-crystal, like by the vibration modes in a molecule. In the Raman light scattering, the vibration modes are regarded as localized, so that the momentum conservation has no need to be considered explicitly. In other words, the Raman-active modes are determined only by their symmetry. The effective supra-crystal polarizability fluctuation at the frequency ν is equal to the nanocrystal polarizability fluctuation $\delta\alpha(\nu)$, multiplied by the number N_{SD} of nanocrystals both in the supra-crystal. Therefore, from above, the intensity of Raman scattering from a supra-crystal containing N_{SD} nanocrystals is proportional to $[N_{SD}L(\nu)\delta^{(1)}\alpha(\nu)]^2$. In consequence, the intensity of Raman scattering from a sample organized into small supra-crystals is expressed as follows:

$$I^{(3)}(\nu) \propto L^2(\nu)[I^{(1)}(\nu)]^2 \qquad (5)$$

Expressions 4 and 5 correspond to two limiting cases: large and small supra-crystals, respectively. However, it is certain that intermediate cases occur, on one hand, when the supra-crystal size is either small or large, and, on the other hand, when there is a mixing of small and large "supra"-crystals. In any case, eqs 4 and 5 allow the establishment of a good cor-
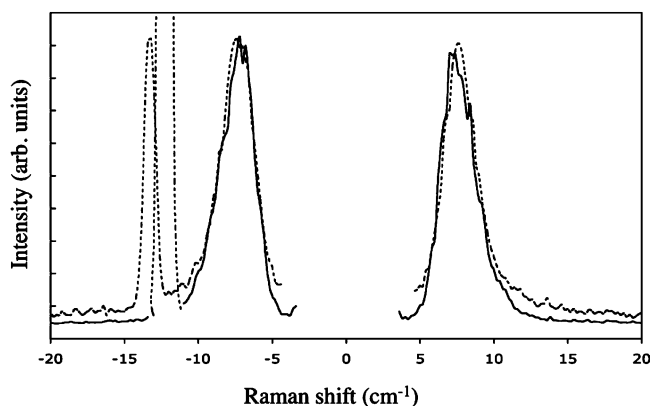
Figure 10. Comparison of the Raman scattered intensity $I^{(3)}(\nu)$ from silver nanocrystals deposited on an amorphous carbon substrate at 22 °C (sample C, dashed line) with the profile $[I^{(1)}(\nu)]^2$ from silver nanocrystals deposited on an HOPG substrate at 10 °C (sample B, solid line). The Stokes and anti-Stokes $I^2(\nu)$ profiles were horizontally shifted and vertically rescaled for the peak maxima to match.

respondence between the X-ray diffraction patterns and the Raman spectra, i.e., between the supra-crystallization and the coherence.

The small-angle X-ray diffraction data explain the observed Raman features.

(A) The first is a *narrowing of the Raman peaks (vibrational coherence)*. The Raman theoretical approach predicts that (1) the narrowing of the Raman lines should only be observed in the case of "small" supra-crystals. This is verified through the comparison of Figures 8B and 9B: while samples C and D both correspond to supra-crystalline arrangements, only sample C shows a narrowing. Therefore, sample C corresponds to "small" supra-crystals. This is precisely what the SAXD patterns show (Figure 2, parts C and D or Figure 3, parts C and D): supra-crystalline organization is less long-ranged in sample C than in sample D; (2) When this narrowing is observed, the line profile is given by the square of that corresponding to a disordered arrangement of nanocrystals. This is illustrated by Figure 10: the narrowed peak of the "small" supra-crystals (sample C) has the same profile as the square of the nonnarrowed peak of the "disordered" sample (sample B). Note that for the latter "disordered" sample, B was chosen and not A, as Figure 8 shows that although both show no supra-crystalline organization, the Raman peak of sample A is somewhat narrowed compared to that of sample B. As noticed in section III.2.a. with the comparison of the Raman line shape with the inverse size distribution, sample A shows signs of vibrational coherence despite its amorphous character deduced from SAXD. This indicates a local arrangement of nanocrystals on a-C (over several particle distances). This allows some vibrational coherence to establish, unlike the arrangement on HOPG. This behavior can be related to a greater supra-crystalline mosaicity on a-C, in contrast to the widespread ordering on HOPG, as supported by the 2D samples (Figure 1, insets): a thorough local ordering over short distances (on a-C) is more relevant than a more widespread but defective ordering (on HOPG), where the phase relationship from one nanocrystal to another is less conserved, for vibrational coherence to settle.

(B) The second is a *shift to low-frequency of the Raman peaks*. In addition to the vibrational coherence narrowing, the theoretical evaluation of the Raman intensity for nanocrystal assemblies predicts a shift of the Raman peak when supra-crystallization occurs, through the appearance of the Lorentz factor $L(\nu)$ in the Raman intensity, regardless of the supra-crystals sizes. The

$L(\nu)$ Lorentz factor[25] (eqs 4 and 5) vary as the inverse of the frequency ν therefore inducing a *low-frequency* shift. This shift is clearly observed for both supra-crystalline samples (Figure 6B and Figure 9A). As remarked above, this shift cannot be explained by the coupling of nanocrystals through the van der Waals interaction between the interdigitized thiol chains. It is interpreted by the Lorentz field and the electromagnetic coherence.

IV. Conclusions

By controlling the substrate and its temperature, it is possible to produce either amorphous aggregates or highly ordered nanocrystals in fcc supra-crystals. Furthermore, the size of the supra-crystals is controlled. Low-frequency Raman scattering detects vibrational coherence. For small supra-crystals, the narrowing of the quadrupolar Raman line manifests coherence. It was shown, in agreement with theoretical predictions, that this narrowing does not exist in large supra-crystals. For any supra-crystals size, the Lorentz field effect, which arises from electromagnetic coherence, is manifested by a shift to low frequency of the quadrupolar Raman line.

References and Notes

(1) Pileni, M. P. *J. Phys. Chem. B* **2001**, *105*, 3358.
(2) Taleb, A.; Petit, C.; Pileni, M. P.; Pileni, M. P. *J. Phys. Chem. B* **1998**, *102*, 2214.
(3) Pinna, N.; Maillard, M.; Courty, A.; Russier, V.; Pileni, M. P. *Phys. Rev. B* **2002**, *66*, 45415.
(4) Maillard, M.; Monchicourt, P.; Pileni, M. P. *Chem. Phys. Lett.* **2003**, *107*, 7492.
(5) Nilius, N.; Benia, H.-M.; Salzemann, C.; Freund, H.-J.; Brioude, A.; Pileni, M.-P. *Chem. Phys. Lett.*, in press.
(6) Petit, C.; Taleb, A.; Pileni, M. P. *Adv. Mater.* **1998**, *10*, 259.
(7) Sun, C. B.; Murray, D.; Weller, L.; Folks, A.; Moser, A. *Science* **2000**, *287*, 1989.
(8) Russier, V.; Petit, C.; Pileni, M. P. *J. App. Phys.* **2003**, *93*, 10001.
(9) Markovich, G.; Collier, C. P.; Heath, J. R. *Phys. Rev. Lett.* **1998**, *80*, 3807.
(10) Taleb, A.; Silly, F.; Gussev, A. O.; Charra, F.; Pileni, M. P. *Adv. Mater.* **2000**, *12*, 633.
(11) Motte, L.; Billoudet, F.; Pileni, M. P. *J. Phys. Chem.* **1995**, *99*, 16425.
(12) Murray, C. B.; Kagan, C. R.; Bawendi, M. G. *Science* **1995**, *270*, 1335.
(13) Brust, M.; Bethell, D.; Schiffrin, D. J.; Kiely, C. *Adv. Mater.* **1995**, *9*, 797.
(14) Harfenist, S. A.; Wang, Z. L.; Alvarez, M. M.; Vezmar, I.; Whetten, R. L. *J. Phys. Chem.* **1996**, *100*, 13904.
(15) Courty, A.; Fermon, C.; Pileni, M. P. *Adv. Mater.* **2001**, *13*, 254.
(16) Lisiecki, I.; Albouy, P. A.; Pileni, M. P. *Adv. Mater.* **2003**, *15*, 712.
(17) Lisiecki, I.; Albouy, P. A.; Pileni, M. P. *J. Phys. Chem. B* **2004**, *108, 20050.*
(18) Germain, V.; Pileni, M. P. *Adv. Mater.* **2005**, *17*, 1424.
(19) Germain, V.; Pileni, M. P. *J. Phys. Chem. B* **2005**, *109*, 5548.
(20) Courty, A.; Mermet, A.; Albouy, P. A.; Duval, E.; Pileni, M. P. *Nat. Mater.* **2005**, *4*, 395.
(21) Brust, M. *Nat. Mater.* **2005**, *4*, 354.
(22) Lisiecki, I.; Albouy, P. A.; Andreaza, C.; Pileni, M. P. Unpublished data.
(23) Duval, E.; Boukenter, A.; Champagnon, B. *Phys. Rev. Lett.* **1986**, *56*, 2052.
(24) Fuiji, M.; Nagareda, T.; Hayashi, S.; Yamamoto, K. *Phys. Rev. B* **1991**, *44*, 6243.
(25) Palpant, B.; Portales, H.; Saviot, L.; Lermé, J.; Prével, B.; Pellarin, M.; Duval, E.; Perez, A.; Broyer, M. *Phys. Rev. B* **1999**, *60*, 17107.
(26) Portales, H.; Saviot, L.; Duval, E.; Fujii, M.; Hayashi, S.; Del Fatti, N.; Vallée, F. *J. Chem. Phys.* **2001**, *115*, 3444.
(27) Duval, E.; Portales, H.; Saviot, L.; Fujii, M.; Sumitomo, K.; Hayashi, S. *Phys. Rev. B* **2001**, *63*, 075405.
(28) Courty, A.; Lisiecki, I.; Pileni, M. P. *J. Chem. Phys.* **2002***, 116*, 8074.
(29) Petit, C.; Lixon, P.; Pileni, M. P. *J. Phys. Chem.* **1993***, 97*, 12974.
(30) Taleb, A.; Petit, C.; Pileni, M. P. *Chem. Mater.* **1997**, *9*, 950.
(31) Courty, A.; Araspin, O.; Fermon, C.; Pileni, M. P. *Langmuir* **2001**, *17*, 1372.
(32) Henry, A. I.; Pileni, M. P. Unpublished data.
(33) Lamb, H. *Proc. London Math. Soc*. **1882**, *13*, 189.
(34) Duval, E. *Phys. Rev. B* **1992**, *46*, 5795.
(35) Duval, E.; Mermet, A.; Courty, A.; Albouy, P. A.; Pileni, M. P. *Phys. Rev. B* **2005**, *72*, 0854395.